ADVANCED FUNCTIONAL MATERIALS
www.afm-journal.de

Ice-Templated, Sustainable Carbon Aerogels with Hierarchically Tailored Channels for Sodium- and Potassium-Ion Batteries

*Jing Wang, Zhen Xu, Jean-Charles Eloi, Maria-Magdalena Titirici, and Stephen J. Eichhorn**

Sodium-ion batteries (SIBs) and potassium-ion batteries (PIBs) are prospective candidates for large-scale energy storage systems cause of their abundant resources. However, unsatisfactory rate and cycling performance of carbon-based anodes present a bottleneck for the applications of SIBs/PIBs due to the large sizes of sodium/potassium ions. Herein, oxygen-doped vertically aligned carbon aerogels (VCAs) with hierarchically tailored channels are synthesized as anodes in SIBs/PIBs via a controllable unidirectional ice-templating technique. VCA-3 (cooling rate of 3 K min^{-1}) delivers the highest reversible capacity of ≈298 mAh g^{-1} at 0.1 C with an excellent cycling performance over 2000 cycles at 0.5 C for SIBs, while VCA-5 manifests a superior capacity of ≈258 mAh g^{-1} at 0.1 C with an 82.7% retention over 1000 cycles at 0.5 C for PIBs. Moreover, their full cells demonstrate the promising potential of VCAs in applications. This novel controllable ice-templating strategy opens unique avenues to tune the construction of hollow aligned channels for shortening ion-transport pathways and ensuring structural integrity. New insights into structure-performance correlations regulated by the cooling rates of an ice-templating strategy and design guidelines for electrodes applicable in multiple energy storage technologies are reported.

1. Introduction

The rapid advancement of emerging portable electronic and electric vehicles (EVs) accompanied by the wide utilization of renewable energy accelerates the development of inexpensive, sustainable, and large-scale energy storage systems.[1] Nevertheless, considering the high cost and the limited reserves of lithium, the large-scale applications of commercial lithium ion batteries (LIBs) are greatly constrained.[2] Moreover, lithium mining is known to cause devastating environmental issues of its own, and has also generated significant human rights issues for local indigenous populations in countries such as Argentina, Bolivia, and Chile within the so-called "Lithium Triangle" as well as in the Democratic Republic of Congo for Co needed at the cathode.[3] In the attempt to decarbonize transport and energy systems, we are in danger of generating other ecological issues associated with its continued extraction.

Sodium-ion batteries (SIBs) and potassium-ion batteries (PIBs) are the appealing alternatives to LIBs owing to their abundant resources (Na with 2.83 wt%, K with 2.09 wt%, and Li with only 0.0017 wt% in the Earth's crust)[4] and similar redox potentials (2.71 V for Na^+/Na, −2.93 V for K^+/K, and −3.04 V for Li^+/Li vs a standard hydrogen electrode).[5] Additionally, both SIBs and PIBs show the identical "rocking-chair" mechanism with that of LIBs, which allows a transfer of material design knowledge from LIBs to SIBs/PIBs.[6] However, the conventional graphitic anode for LIBs is not satisfactory for SIBs owing to the absence of stable Na-C binary compounds.[7] Due to the larger ionic radius of K^+ (1.38 Å) compared to Li^+ (0.76 Å), the intercalation/deintercalation of K^+ ions into graphite layers (3.35 Å for graphite interlayer spacing) causes substantial volumetric expansion and "sluggish" kinetics, along with structural degradation, inferior cycling stability, and unfavorable rate capabilities.[8] Therefore, the development of SIBs/PIBs faces a major challenge in exploiting suitable anode materials which can stably and quickly accommodate Na^+/K^+ during the charge–discharge process for achieving enhanced cycling and rate performances.[9]

J. Wang, S. J. Eichhorn
Bristol Composites Institute
School of Civil
Aerospace, and Mechanical Engineering
University of Bristol
University Walk, Bristol BS8 1TR, UK
E-mail: s.j.eichhorn@bristol.ac.uk
Z. Xu, M.-M. Titirici
Department of Chemical Engineering
Imperial College London
South Kensington Campus, London SW7 2AZ, UK
J.-C. Eloi
School of Chemistry
University of Bristol
Cantock's Close, Bristol BS8 1TS, UK

The ORCID identification number(s) for the author(s) of this article can be found under https://doi.org/10.1002/adfm.202110862.

DOI: 10.1002/adfm.202110862

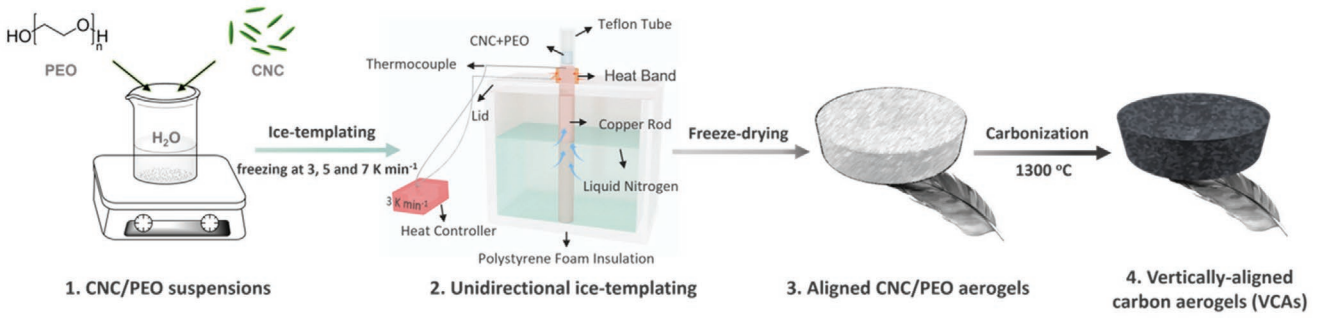

Scheme 1. Schematic of the synthesis process of CNC/PEO-derived VCAs anodes for SIBs/PIBs.

Apart from graphitic carbon, non-graphitic hard carbon possesses a disordered structure still containing some crystalline domains with a larger interlayer spacing, facilitating Na^+/K^+ diffusion.[10] Thus, extensive research has focused on micro/nanostructured hard carbons as appropriate anode materials for SIBs/PIBs over the past few years.[11] It is well known that ice-templating, also called "freeze-casting," comprises the freezing of a suspension, followed by the sublimation of the ice crystals which are a template for the ultimate pores.[12] Among a variety of strategies for producing micro/nanostructured materials, ice-templating is an expeditious and highly adaptable technique to construct aligned and hierarchical channels in the case of unidirectional freezing.[13] Recently, Cui et al.[14] adopted a unidirectional ice-templating strategy to fabricate low-tortuosity, vertically aligned reduced graphene oxide as Li-metal host anodes. They demonstrated that vertically aligned channels have a positive impact on shortening the ionic or mass transportation path, thus accordingly improving diffusion kinetics and cycling performance. To date, the employment potential of unidirectional ice-templating strategies on the anode field for SIBs/PIBs remains unexplored and unidentified. Equally importantly, resources availability is expected to be of great significance for the large-scale production of devices. As an appealing alternative to costly and non-biodegradable materials (e.g., graphene and carbon nanotubes), cellulose nanocrystals (CNCs) are extracted from natural cellulose-based biomass, which is a potentially biodegradable nanomaterial with large-scale availability at comparatively low cost.[15]

In this work, we innovatively develop a controllable unidirectional ice-templating strategy (**Scheme 1**) to tailor low-cost CNC/polyethylene oxide (PEO)-derived, vertically aligned carbon aerogels (VCAs) anodes with desirable features for the large-scale practical applications of SIBs/PIBs. Our material design integrates the following merits: i) fine-tuning of the interlayer spacing and channel width to facilitate ion diffusion through the regulation of cooling rates; ii) hierarchically tailored and vertically aligned channels acting as ion reservoirs to boost electrolyte percolation and a carbon skeleton to buffer volume change simultaneously; iii) doping of oxygen functional groups to offer more electrochemically active sites. To the best of our knowledge, this is the very first report on VCA anodes with enhanced rates and cycling capabilities of SIBs/PIBs by controlling the cooling rate of a unidirectional ice-templating technique.

2. Results and Discussion

Figure 1a illustrates the principle of the controllable unidirectional ice-templating process. The CNCs and the low-cost PEO binder are dispersed in water and then cast in a mold sitting on the top of a cold finger in contact with a liquid-nitrogen bath (Step 1). Afterward, the ice crystals unidirectionally grow along the temperature gradient. Meanwhile, the dispersed nanoparticles are expelled from the forming anisotropic ice crystals (Step 2). Under the controlled and constant cooling rates (i.e., 3, 5, and 7 K min^{-1}), the corresponding speed of the freezing ice front or the freezing kinetics is precisely regulated.[16] During the subsequent freeze-drying process, the anisotropic ice crystals are sublimated to eventually generate vertically aligned channels surrounded by the concentrated CNC/PEO nanoparticle walls (Step 3). After further carbonization of the aligned CNC/PEO aerogels, the VCAs can be fabricated with vertically aligned channels and sodiophilic/potassiophilic conductive carbon aerogels walls (Step 4). We have produced ice-templated, lightweight, sustainable CNC-based nanocomposite aerogels and carbonized dense aerogels (Figure 1b).

The as-formed CNC/PEO aerogels have a range of densities from 17.8 to 28.3 mg cm^{-3} (Table S1, Supporting Information), which are lower than the densities of reported conventional randomly arranged CNC-based aerogels (122.0 mg cm^{-3}) via all-directional freezing.[17] The vertically aligned, channeled microstructure of the CNC/PEO nanocomposite aerogels was first revealed by cross-sectional scanning electron microscopy (SEM, Figure 1c), presenting millimeter-scale continuous vertical alignment. Typically, the top-view SEM image exhibits a honeycomb-like cellular structure in the inset (Figure 1c). This microstructural analysis is consistent with 3D reconstructions from X-ray tomography (Figure 1d) which illuminates millimeter-long aligned tubular channels parallel to the freezing direction throughout the aerogel. The corresponding top-view of the 3D computed tomography reconstruction shows the uniform cellular channels and the presence of channel interconnectivity. Furthermore, a more densely packed honeycomb-like cellular architecture perpendicular to the ice crystal growth is revealed by the SEM images of the VCAs (Figure 1e,f). It is observed that VCA-3, -5, and-7 exhibit uniform and smaller cellular channels (i.e., macropores) with a higher homogeneity, in contrast to VCA-U that has irregular and larger cellular channels with a noncontinuous structure (Figure S1, Supporting Information). Based on these observations, we can conclude that the higher

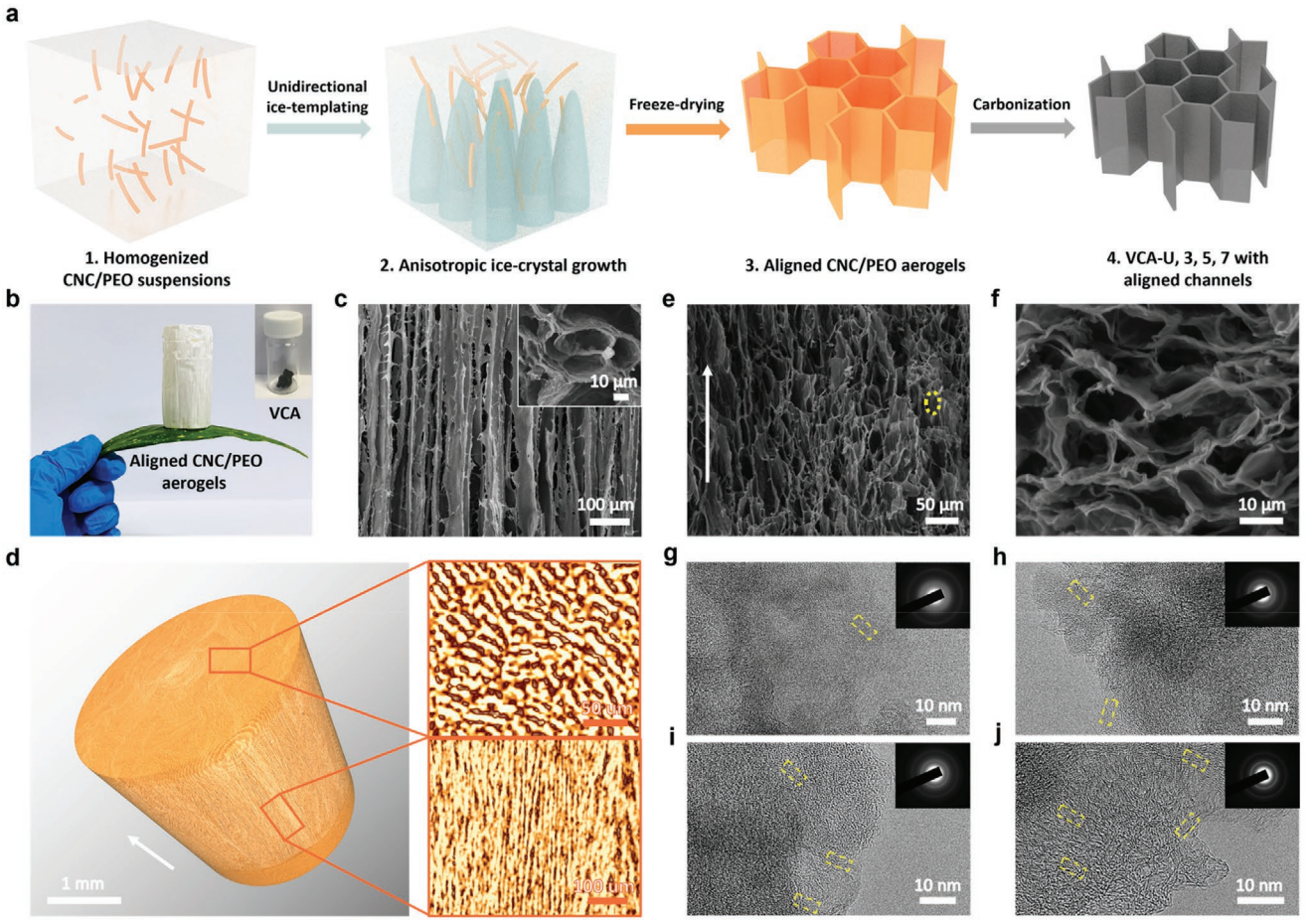

Figure 1. a) Schematic illustrating the formation mechanism of unidirectional ice-templated VCAs. b) A photograph showing an aligned CNC/PEO aerogel standing on a leaf; the inset is a digital photograph of the VCA. c) Typical SEM images of a cross-sectional and top-view (inset) of the CNC/PEO aerogels. d) 3D reconstructions of honeycomb-like cellular pores derived from X-ray tomography. SEM images of e) VCA-7 from the longitudinal view and f) VCA-7 from the top view. HRTEM images and inset SAED patterns of g) VCA-U, h) VCA-3, i) VCA-5, and j) VCA-7. The freezing direction in (d) and (e) is indicated by white arrows.

cooling rate can result in smaller and finer vertically-aligned channels of VCAs, which decreases to 19.7 μm (VCA-7) from 47.9 μm (VCA-3) (Table S2, Supporting Information).

The nanostructures of VCAs were investigated by high-resolution transmission electron microscopy (HRTEM) as shown in Figure 1g–j. Generally, there are more turbostratic carbon structures and fewer graphitic ordered domains in VCA-U compared with those of the controlled VCAs (yellow dashed rectangle denotes ordered domains). It is obvious that with an increasing cooling rate from 3 to 7 K min^{-1}, short-range ordered nanodomains with a higher content of graphitic structures were observed. The selected area electron diffraction (SAED) patterns displayed dispersed diffraction rings and no diffraction spots for all the VCA samples (inset in Figure 1g–j). The diffraction rings are initially diffuse for VCA-U, but become sharper for VCA-7, suggesting a further increase of the ordering of the crystalline carbon structures with elevated cooling rates. It was also observed that the unidirectional freezing synchronously induced the orientation of highly crystalline and rod-shaped CNCs (Figure S2, Supporting Information); this can assist in retaining the short-range ordered structures in VCAs. This hierarchically ordered structure is thought to be instrumental in conveying the unique hierarchically-tailored properties of our materials.

X-ray diffraction (XRD) patterns of all VCAs exhibit two broad peaks centered at $2\theta \approx 22°$ and 43°, corresponding to the (002) and (100) planes of expanded graphite (**Figure 2**a). In our VCAs, the calculated average interlayer spacing (d_{002}) of graphite layers are found using Bragg's law (Equation S2, Supporting Information) as shown in Figure 2d. The reduction in the full width at half-maximum (FWHM) of the (002) Bragg reflection from VCA-U to VCA-7 is indicative of a more ordered structure. With a decrease in the cooling rate, the (002) Bragg reflections of VCA-7, -5, and -3 are redshifted to a lower diffraction angle, which suggests an enlargement of the interlayer spacing (Figure S4, Supporting Information).[18] Figure 2b and Figure S5, Supporting Information show Raman spectra of VCAs, presenting the two characteristic D- and G-bands located at ≈1340 and ≈1580 cm^{-1}, respectively. Differing from ordered graphitic carbons (Stage 1), all these VCAs pertain to Stage 2 of the classic three-stage Raman model proposed by Ferrari et al.,[19] which is specifically applied to amorphous carbons

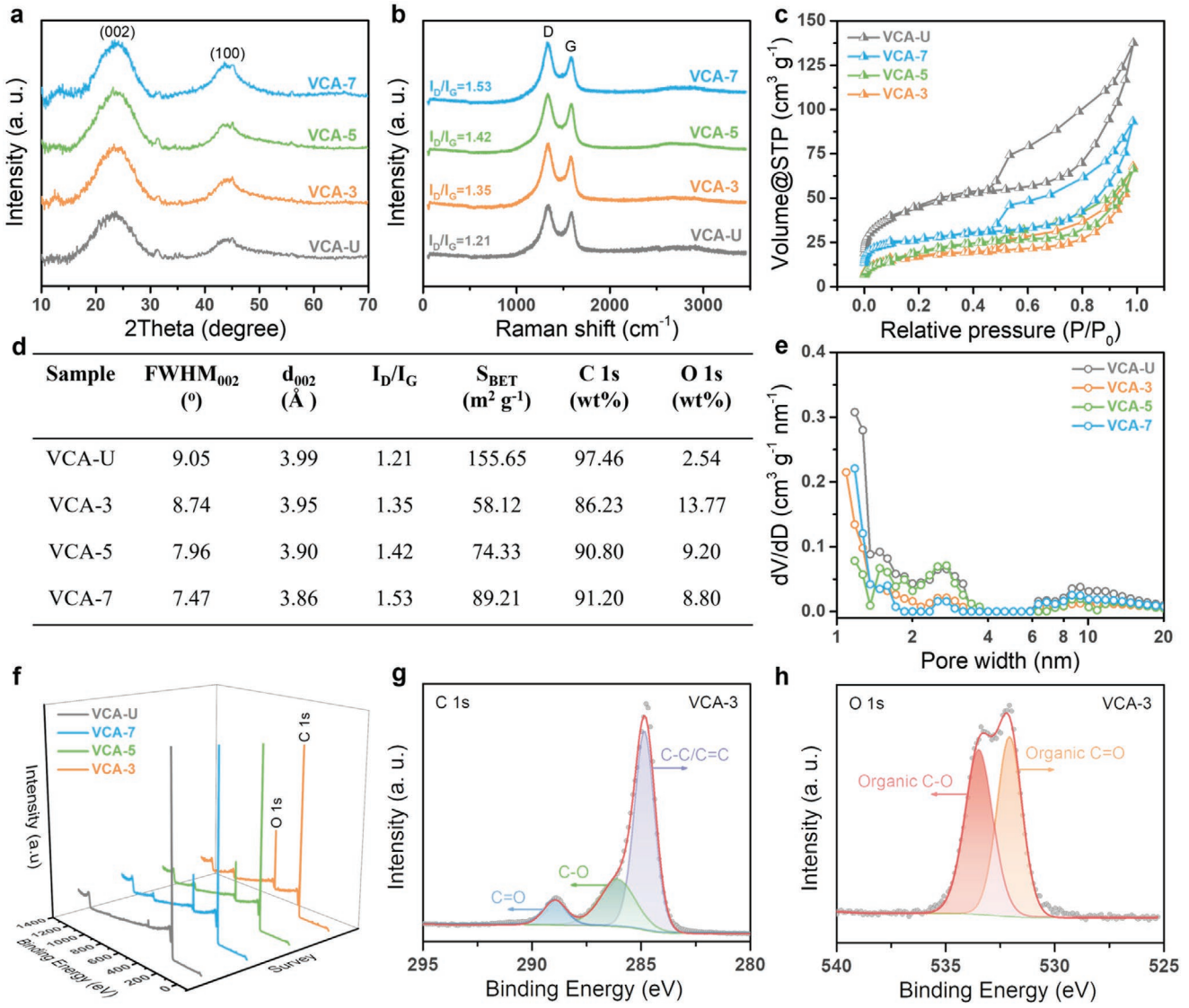

Sample	$FWHM_{002}$ (°)	d_{002} (Å)	I_D/I_G	S_{BET} (m^2 g^{-1})	C 1s (wt%)	O 1s (wt%)
VCA-U	9.05	3.99	1.21	155.65	97.46	2.54
VCA-3	8.74	3.95	1.35	58.12	86.23	13.77
VCA-5	7.96	3.90	1.42	74.33	90.80	9.20
VCA-7	7.47	3.86	1.53	89.21	91.20	8.80

Figure 2. a) XRD patterns, b) Raman spectra, c) nitrogen adsorption-desorption isotherms, and e) pore size distributions. d) Summary of structural and surface elemental parameters, and f) full XPS survey spectra of VCA-U, -3, -5, and -7. High-resolution XPS spectra of g) C 1s and h) O 1s core levels for VCA-3 (a.u. = arbitrary units).

with a high defect density when the average inter-defect distance (L_D) is less than 3 nm. More importantly, the intensity ratio (I_D/I_G), which is proportional to the number of ordered hexagons (M) or the square of L_D at Stage 2, increases with a decreasing number of defects within the graphite layers. Hence, the ratio of I_D/I_G of VCA-U, VCA-3, VCA-5, and VCA-7 gradually increases, which results from their increasing crystallinity or the degree of ordering, and a decrease in the defect density within the graphitic layers.[20] The results of XRD and Raman spectroscopy are consistent with HRTEM observations, which further confirms that our ice-templating strategy, with the controlled cooling rate, can introduce relatively more ordered graphitic structures; namely, increasing cooling rates results in a higher degree of ordering but a smaller interlayer spacing. Based on the analysis of HRTEM and SAED images (Figure 1g–j), XRD patterns (Figure 2a), and Raman spectra (Figure 2b), VCA-3 shows fewer short-range graphitic nanodomains but more defects; conversely VCA-7 shows more short-range graphitic nanodomains but fewer defects; VCA-5 possess a medium number of short-range graphitic nanodomains and the requisite number of defects. The calculated L_D values are presented in Table S2, Supporting Information, as determined using Equation S3, Supporting Information.

Typical type IV nitrogen adsorption/desorption isotherms with hysteresis loops are observed for all four samples, indicating the presence of mesopores (Figure 2c). The VCA-U sample shows the highest Brunauer–Emmett–Teller (BET) specific surface area (S_{BET}) of 155.65 m^2 g^{-1} with a pore volume of 0.161 cm^3 g^{-1} after high-temperature carbonization. Based on the control of the cooling rates, the resulting VCA-3, -5, and -7 samples exhibit S_{BET} values ranging from 58.12 to 89.21 m^2 g^{-1}, with a small fluctuation in pore volume between 0.081 and

0.109 cm^3 g^{-1}. The pore size distributions and average pore diameters are shown in Figure 2e and Table S2, Supporting Information, revealing that unidirectional ice-templating facilitates the formation of hierarchical pores including a few micropores (<2 nm) and dominant mesopores (2–50 nm). X-ray photoelectron spectroscopy (XPS) measurements were employed to probe the elemental composition of samples, as summarized in Figure 2d. XPS spectra from all samples (Figure 2f) show two pronounced peaks located at ≈284 and ≈532 eV, attributed to the core level of C1s and O1s, respectively. These data indicate that the VCA-3 possesses the highest oxygen content among all the samples; this confirms the composition of carbon (86.23 wt%) and oxygen (13.77 wt%). The high-resolution C1s spectrum of VCA-3 (Figure 2g) is deconvoluted into peaks representing C—C, C—O, and C=O; these peaks are located at 284.82, 286.06, and 288.95 eV, respectively. The deconvoluted O1s spectra of VCA-3 (Figure 2h) revealed the presence of two different bands with binding energies of 532.07 and 533.46 eV, corresponding to the organic C=O and C—O moieties, respectively. The C1s and O1s deconvolutions of other VCAs are presented in Figure S6, Supporting Information. It has been demonstrated that oxygen functional groups can generate defective sites and structural vacancies in favor of the adsorption of Na^+/K^+.[21]

The sodium storage capability of the VCA electrodes was investigated in half coin cells with metallic Na as the counter electrode. The cyclic voltammetry (CV) analysis of half cells was conducted at a scan rate of 0.1 mV s^{-1} in the voltage window of 0.01–2.5 V (vs Na^+/Na). In the first three consecutive cyclic voltammograms of the VCA-3 electrode (**Figure 3**a), two broad cathodic peaks at ≈0.4 and ≈1.1 V are visible in the first cycle but disappear in the following two scans. This can be attributed to the decomposition of the electrolyte and the formation of the solid electrolyte interphase (SEI) layer on the electrode surface, whereafter the overlap of CV curves in the subsequent cycles implies the high reversibility of the VCA-3 electrodes for Na^+ ion storage. It can be seen from Figure 3b that the initial capacity loss of the VCA-U electrode is larger than that of VCA-3. The area covered by CV curves for VCA-3 is much wider than those of VCA-U, VCA-5, and VCA-7 (Figure S7a,b, Supporting Information), suggesting the increased sodium-ion storage capability of VCA-3. Figure 3c shows the galvanostatic charge/discharge (GCD) profiles of VCA-U, -3, -5, and -7 in the second cycle between 0.01 and 2.5 V (vs Na^+/Na). All VCA electrodes exhibit two potential regions, the sloping region from 1.2 to 0.1 V is termed as the Na^+ ion adsorption onto the surface-active sites (e.g., defective sites, functional groups, and surfaces); moreover, the plateau region at around 0.1 V corresponds to the Na^+ filling into nanovoids, which has been proven by our previous research using ex situ ^{23}Na solid-state NMR spectroscopy, small and wide angle X-ray scattering, and density functional theory (DFT) calculations.[22] It is worth noting that VCA-3 delivers the highest reversible charge capacity of 298 mAh g^{-1} at a current density of 30 mA g^{-1} with the largest high-potential sloping region among all four kinds of VCA electrodes. In contrast, the VCA-U electrode exhibits a reversible charge capacity of only 197 mAh g^{-1} at the same current density. The low initial Coulombic efficiency (ICE) of VCA-U (44%) can be related to the excessive formation of the SEI layer caused by its relatively high S_{BET} (155.65 m^2 g^{-1}) and porosity.[23] The optimized microstructures of VCA-3 with relatively smaller and uniformly distributed cellular channels greatly reduce its surface area (58.12 m^2 g^{-1}), thereby decreasing the initial capacity loss.[24]

Figure 3d compares the rate performance of VCA-U, -3, -5, and -7 electrodes for SIBs at various current densities from 0.1 to 2.0 C (1 C for 300 mA g^{-1} confirmed by the reversible capacity of hard carbon[25]). VCA-3 exhibits an outstanding reversible capacity and rate performance among all these VCAs. At a high current density of 1.0 C, the high reversible capacity of VCA-3 reaches 209 mA g^{-1} compared to VCA-7 (192 mA g^{-1}), VCA-5 (156 mA g^{-1}), and VCA-U (79 mA g^{-1}). The reversible capacity of VCA-3 maintains ≈290 mA g^{-1} when the current density is reverted to 0.1 C after 25 cycles, which reflects a superior rate capability and reversibility of the VCA-3 electrode. This phenomenon can be attributed to the presence of the hierarchically tailored channels and favorable uniformity of VCA-3, which facilitates the electrolyte permeation and fast ion transport upon using higher current densities. The cycling stability was evaluated at a current density of 0.5 C and is presented in Figure 3e. The VCA-U delivers a low reversible capacity of only 107 mA g^{-1} after 200 charge/discharge cycles in contrast to VCA-7 (190 mA g^{-1}) and VCA-5 (180 mA g^{-1}). The VCA-3 holds a higher reversible capacity of 220 mA g^{-1} after 200 cycles with a nearly 100% Coulombic efficiency, signifying the superior cycling stability with a 91.5% capacity retention. When cycled at 2.0 C, the reversible capacity of the VCA-3 electrode can remain at ≈105 mAh g^{-1} after 100 cycles of the sodiation/desodiation processes with a Coulombic efficiency of nearly 100%, corresponding to a capacity retention of 85.0% (Figure S15a, Supporting Information). Moreover, extended cycling tests up to 2000 cycles were further conducted at 0.5 C (Figure S7c, Supporting Information). The VCA-U almost delivers no capacity after 450 cycles, while the VCA-3 shows a decay of 0.03% per cycle during 2000 cycles with an excellent Coulombic efficiency of 99.9%, highlighting the stable electrochemical performance of VCA-3 electrode for the long-term cycling life. The superior sodium storage performance of VCA-3 benefits from the synergistic effects of plentiful oxygen-doping active sites (O content of 13.77 wt%) and more defects within graphitic layers to facilitate the adsorption of Na^+. Besides, the homogenous vertically aligned and large hollow channels not only effectively reduce the ion-transportation pathway, but also accommodate the volume expansions to preserve the structural integrity during long-term cycling.[26]

Additionally, the potassium storage properties of the four electrodes in half cells were also evaluated in the potential range between 0.01 and 2.5 V (vs K^+/K). **Figure 4**a shows the CV analysis of VCA-5 at 0.1 mV s^{-1}, indicating a prominent reduction peak at 0.64 V in the first discharge cycle due to the formation of an SEI film on the surface of the electrode. A pair of redox peaks at a low potential range of 0.01–0.5 V can be observed, corresponding to the insertion/extraction of K^+ into the VCA electrodes. No significant changes in the CV curves are observed during the subsequent cycles except for the disappearance of the cathodic peak at 0.64 V. It is obvious that VCA-U contains a substantial irreversible capacity decay in the first cycle (Figure 4b), as well as a smaller area of the CV curve compared with VCA-3

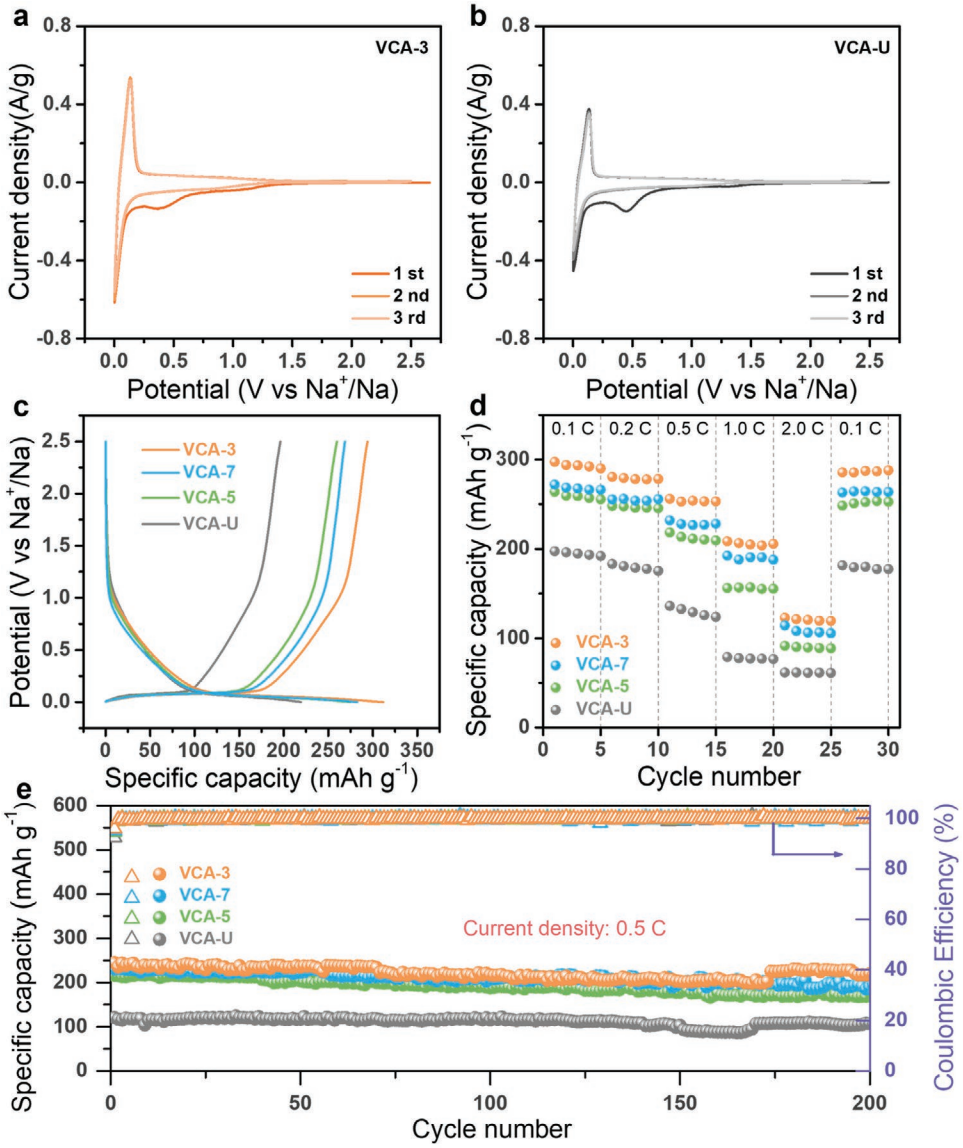

Figure 3. Electrochemical properties of VCA electrodes in half cells of SIBs. Cyclic voltammetry curves of a) VCA-U and b) VCA-3 at a scan rate of 0.1 mV s^{-1}. c) Galvanostatic charge–discharge profiles of the second cycle. d) Rate capability at various current densities from 0.1 to 2.0 C. e) Cycling performance at a current density of 0.5 C (1 C = 300 mA g^{-1}).

and VCA-7 (Figure S8, Supporting Information). Figure 4c presents the GCD profiles of the VCA-U, -3, -5, and -7 electrodes in the second cycle at the current density of 0.1 C (1 C equal to 279 mA g^{-1} calculated based on the theoretical capacity of KC_8[27]) between 0.01 and 2.5 V (vs K^+/K). As observed in Figure 4c, the potential of the sloping region is larger than ≈0.3 V, which indicates a capacitive-controlled process; this refers to the K^+ ion adsorption on the defective sites, edges, or surfaces. VCA-U delivers a reversible charge capacity of 191 mA g^{-1} at 0.1 C with a very low ICE of 34%. On the contrary, the ICEs of VCA-3, -5, and -7 electrodes are expected to be enhanced by the controlled cooling rates of the unidirectional ice-templating technique, which is consistent with the results of the CV curves. Generally, the ICE could be further improved by the optimization of the electrolyte systems and pre-potassiation.[28]

Figure 4d reveals the rate capability of the VCAs at different current densities for PIBs. VCA-5 delivers the highest charge capacities of 258 mA g^{-1} at the current density of 0.1 C. Moreover, the rate performance of VCA-5 outperforms other VCAs upon higher charge/discharge current densities. It exhibits a reversible capacity of 148 mA g^{-1} at a current density of 2.0 C, which is higher than VCA-3 (133 mA g^{-1}), VCA-7 (113 mA g^{-1}), and VCA-U (83 mA g^{-1}). On returning to a lower current density of 0.1 C, VCA-5 undergoes an increase in reversible capacity up to 260 mA g^{-1}, which confirms the outstanding reversibility of the VCA-5 electrode. As for the cycling stability, VCA-5 also overtakes all other VCA electrodes for PIBs (Figure 4e). The VCA-5 holds a reversible capacity of 173 mA g^{-1} after 300 cycles at 0.5 C, which corresponds to an excellent capacity retention of 90.2%. In comparison, the capacity of VCA-U fades from

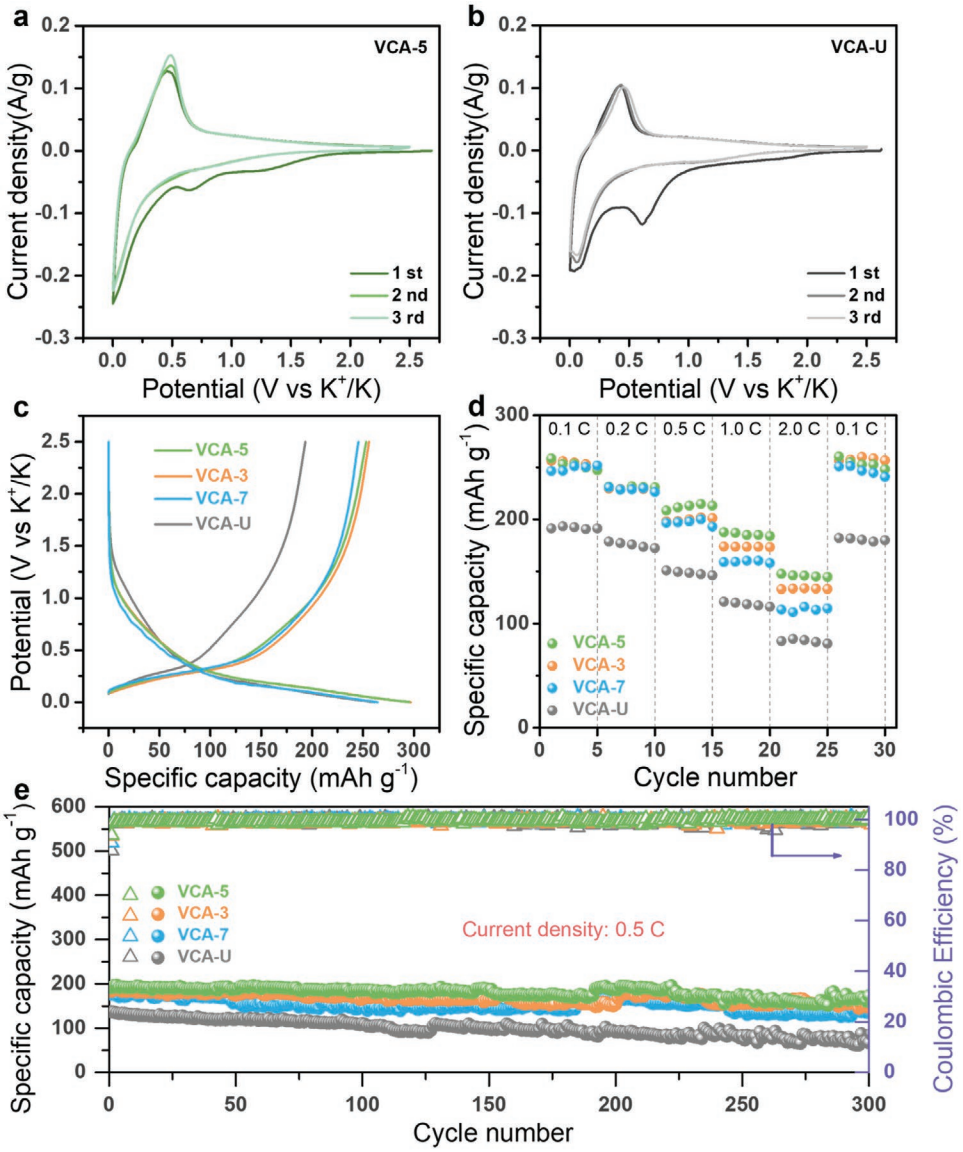

Figure 4. Electrochemical properties of VCA electrodes in half cells of PIBs. Cyclic voltammetry curves of a) VCA-U and b) VCA-5 at a scan rate of 0.1 mV s^{-1}. c) Galvanostatic charge–discharge profiles of the second cycle. d) Rate capability at various current densities from 0.1 to 2.0 C. e) Cycling performance at a current density of 0.5 C (1 C = 279 mA g^{-1}).

137 to 91 mA g^{-1} ascribed to a capacity retention of only 66.4%. The VCA-3 and VCA-7 electrodes exhibit higher retentions of 83.3% and 73.4%, respectively. Notably, a reversible capacity of ≈135 mAh g^{-1} for the VCA-5 electrode can be still obtained after 100 potassiation/depotassiation cycles at a high current density of 2.0 C, approaching a high-capacity retention of 90.6% and a Coulombic efficiency of 99.9% (Figure S15b, Supporting Information). The long-term cycling stability was also evaluated at 0.5 C for 1000 cycles (Figure S8c, Supporting Information). The massive capacity loss of VCA-U occurs at the 530th cycle with an ultralow capacity of ≈30 mA g^{-1}, implying the existence of its structural collapse arising from the mechanical stress/strain during the insertion process of large-sized K^+ ions.[29] Conversely, VCA-5 exhibits an extraordinary long-cycle performance (151 mAh g^{-1} at 0.5 C after 1000 cycles), unprecedented capacity retention (82.7%) and a high Coulombic efficiency (≈100%). The preeminent rate capability and cycling stability of VCA-5 in PIBs benefits from the subsequent points: 1) the rigid hollow channels can shorten the diffusion pathway, promote electrolyte/electrode contact area, and alleviate the volume change; 2) the moderate defects and oxygen-functional groups can offer some active sites; 3) the more graphitic nanodomains with an enlarged interlayer spacing (0.39 nm) can facilitate the effective insertion/extraction of K^+ ions.[30]

To gain further insight into the sodium ion storage mechanisms, it is imperative to illuminate the contribution of two major mechanisms, namely, capacitive- and diffusion-controlled processes.[31] Specifically, the behavior of Na^+ ion adsorption onto surface defects is defined as a surface-induced pseudocapacitive process, and the Na^+ ion insertion into nanovoids is a

diffusion-controlled process. The VCA electrodes were scanned at different sweep rates ranging from 0.1 to 5.0 mV s^{-1}, as shown in **Figure 5**a (see Figure S9a–c, Supporting Information for the CV curves of the VCA-U, VCA-5, and VCA-7 electrodes). Based on a power-law formula ($i = av^b$), the ratio of capacitive- and diffusion-controlled capacity contributions was quantitatively calculated using the equation

$$i(V) = k_1 v + k_2 v^{\frac{1}{2}} \quad (1)$$

as has been reported by several researchers;[32] if the current response (i) at a specific potential (V) can be regarded as a mixture of the aforementioned two types of charge storage mechanisms, then $k_1 v$ and $k_2 v^{\frac{1}{2}}$ represent the capacitive-controlled (fitted in red area) and diffusion-controlled (blue area) contributions, respectively. Accordingly, Figure 5b and Figure S13a, Supporting Information display the typical CV curve at a specific scan rate (0.5 mV s^{-1}), in which the fitted red area represents the capacitive-controlled contributions to the overall capacities of VCA-U (46%) and VCA-3 (50%), respectively. As the sweep rate ranges from 0.1 to 5.0 mV s^{-1}, the capacitive contribution of VCA-3 gradually increases from 31% to 96% (Figure 5c). In comparison, the VCA-U shows a relatively lower proportion of capacity contributed by the capacitive behavior of 26% at 0.1 mV s^{-1} and 80% at 5.0 mV s^{-1} (Figure S9d, Supporting Information). Therefore, these results can be correlated to the favorable rate performance of VCA-3 for SIBs, because its continuously increased capacitive-controlled contributions originate from the pseudo-capacitance reactions with faster kinetics.

Moreover, according to the electrochemical impedance spectroscopy (EIS) of half cells employing VCA-U, -3, -5, and -7 electrodes at the de-sodiated states, VCA-3 shows the lowest charge-transfer resistance (R_{ct}) compared to other samples in

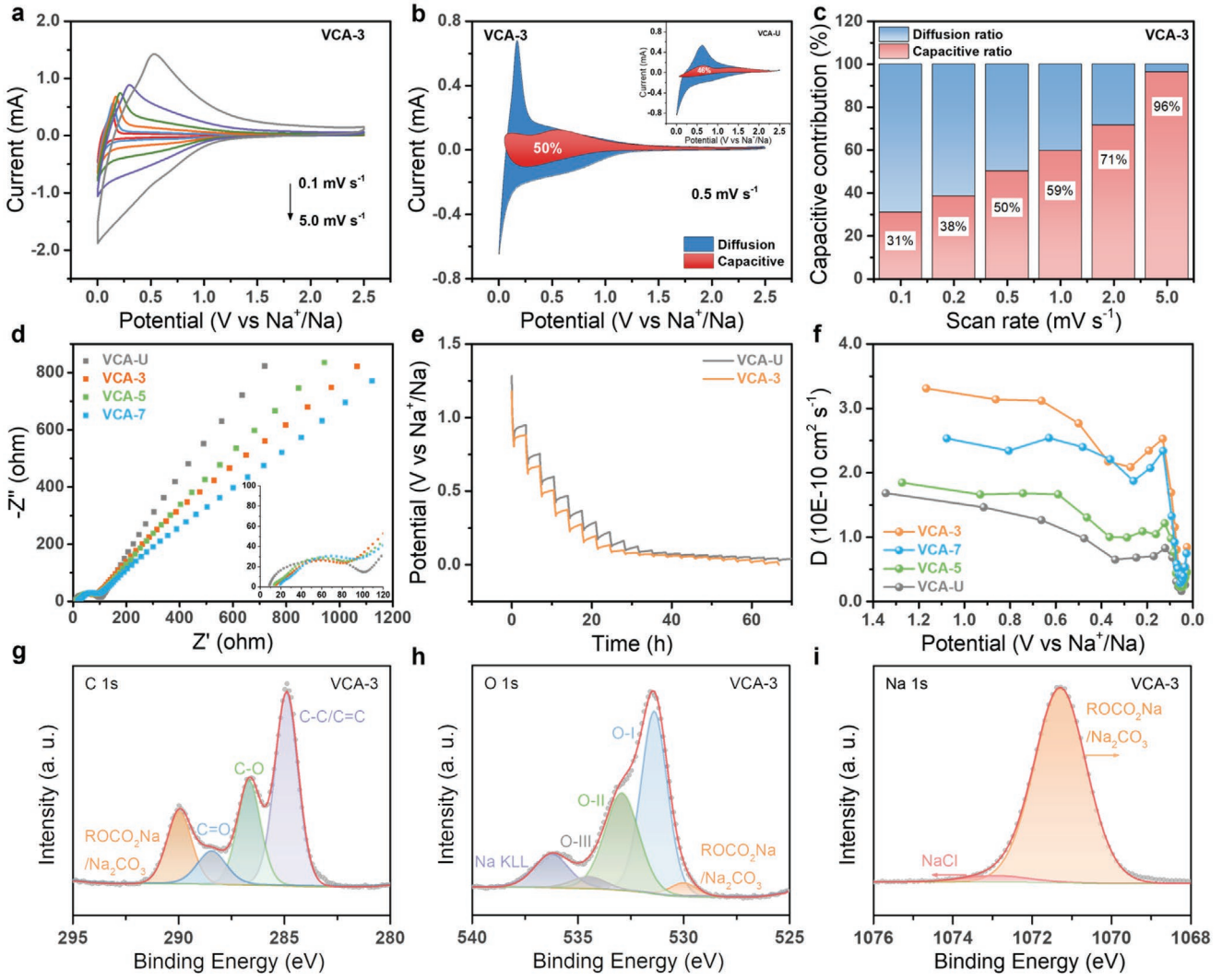

Figure 5. SIB analysis: a) CV curves at various scan rates from 0.1 to 5.0 mV s^{-1}. b) Separation of the capacitive and diffusion-controlled charges at 0.5 mV s^{-1}. c) Contribution ratios of the capacitive and diffusion-controlled charge at various scan rates. d) EIS analysis. e) GITT potential profiles of the discharging process. f) The sodium ion diffusion coefficients as a function of the state of the discharging process. Ex situ XPS spectra of g) fitted C 1s, h) O 1s, and i) Na 1s core levels for the cycled electrode.

the half cell configuration of SIBs (Figure 5d; Table S3, Supporting Information). This demonstrates that the VCA-3 electrode has the highest charge-transfer kinetics during the sodiation/desodiation process due to rich oxygen functional groups-derived active sites, large amounts of intrinsic defects, and a favorably uniform and hollow channel network.[29,33] The electrochemical kinetics were further investigated using galvanostatic intermittent titration (GITT) measurements to estimate the diffusion coefficients of Na^+ ions for VCA electrodes (Figure 5e,f; Figure S10, Supporting Information). As shown in Figure 5e, the VCA-3 electrode displays smaller overpotentials than the VCA-U electrode, signifying its higher Na^+ diffusion coefficient (D_{Na^+}). Values of D_{Na^+} can be determined by applying a simplified version of Fick's second law:[34]

$$D = \frac{4}{\pi\tau}\left(\frac{m_b V_M}{M_B S}\right)^2\left(\frac{\Delta E_s}{\Delta E_\tau}\right)^2\left(\tau \ll \frac{L^2}{D}\right) \quad (2)$$

where τ is the current pulse time, m_b, M_B, and V_M are the mass, the molar mass, and the molar volume of active materials; S is the area of the electrode; ΔE_τ and ΔE_s are the potential changes at τ and relaxation stages per GITT step, respectively. The calculated results of the D_{Na^+} values are plotted as shown in Figure 5f. First of all, the average D_{Na^+} value in the sloping region (>0.1 V vs Na^+/Na) is much higher than that in the plateau region (<0.1 V vs Na^+/Na), which means that the sloping capacity is dominated by the capacitive-controlled behaviors with the faster kinetics, while the plateau capacity is mainly derived from the diffusion-controlled behaviors with slower kinetics. Moreover, it is noteworthy that VCA-3 shows the highest average D_{Na^+} value among four VCA electrodes based on the same active mass, which demonstrates faster Na^+ ion diffusion coefficients in VCA-3. The aforementioned results can be ascribed to the hierarchical channels and more active sites derived from the oxygen-doping of VCA-3, agreeing well with its superior electrochemical properties.

When it comes to PIB analysis, **Figure 6**a shows the CV curves of VCA-5 under various sweep rates for PIBs (Figure S11a–c, Supporting Information for the CV curves of the VCA-U, VCA-3, and VCA-7 electrodes). Based on quantitative calculations from CV curves, 40% of the total charge storage for the VCA-5 electrode is capacitive at the sweep rate of 0.5 mV s^{-1}, which is higher than 34% for the VCA-U electrode (Figure 6b; Figure S13b, Supporting Information). The proportions of the capacitive contribution of VCA-5 at different scan rates from 0.1 to 5.0 mV s^{-1} are concluded in Figure 6c, which exhibits a gradually increasing ratio from 26% to 84%. In contrast, VCA-U has the 24% and 71% capacitance contribution at 0.1 and 5.0 mV s^{-1}, respectively (Figure S11d, Supporting Information). Such a higher proportion of capacitive contribution along with the faster electrochemical kinetic account for the superior rate performance and structural stability of the VCA-5 electrode in PIBs. Figure 6d shows the Nyquist plots of VCA electrodes from EIS analysis, where VCA-5 displays the smallest R_{ct} in comparison with VCA-3, VCA-7, and VCA-U (Table S3, Supporting Information) in half cells of PIBs. It demonstrates that the VCA-5 electrode possesses the lowest charge-transfer resistance at the electrode/electrolyte interface during the potassiation/depotassiation process, which can be attributed to the enhanced number of short-range ordered nanodomains with an expanded interlayer spacing, the appropriate number of defective sites and well-developed hollow channels.[35] To further illustrate the K^+ ion diffusion kinetics of VCA electrodes, GITT measurements were conducted as well (Figure 6e,f; Figure S12, Supporting Information). Compared to the VCA-U electrode, the VCA-5 electrode exhibits a higher K^+ ion diffusion coefficient (D_{K^+}) as a result of smaller overpotentials during the discharging process.[36] The quantitative calculations of D_{K^+} as a function of potential were obtained using Equation (2), as displayed in Figure 6f. Similar to SIBs, the average D_{K^+} value in the sloping region (>0.3 V vs K^+/K) is much higher than that in the plateau region (<0.3 V vs K^+/K), which means that the sloping capacity is also dominated by the capacitive-controlled behaviors with the faster kinetics, while the plateau capacity is derived from the diffusion-controlled behaviors with the slower kinetics as well. Intriguingly, a similar trend is found for these four VCA electrodes, but VCA-5 outperforms other VCA electrodes in terms of the D_{K^+} value at all potentials. This trend suggests an enhanced ion diffusion pathway during the de/potassiation of VCA-5, owing to its enlarged spacing interlayer spacing and the well-developed aligned channels, which is in good agreement with the EIS analysis above.

To comprehend the interface of the cycled electrodes, ex situ XPS investigations were performed to systematically analyze the nature and chemical compositions of SEI layers formed in SIBs and PIBs. The XPS spectra were collected on the outermost SEI layers of VCA-3 in $NaClO_4$-based electrolytes and VCA-5 in KPF_6-based electrolytes after the initial discharge and charge cycle, as shown in Figures 5g–i,6g–i. According to high-resolution XPS spectra of O 1s in both cases (Figures 5h,6h), three observed peaks located at ≈531.5, ≈532.9, and ≈534.5 eV are designated as C=O carbonyl groups (O-I), C−OH hydroxyl or C−O−C ether groups (O-II), and O=C−OH carboxyl groups (O-III).[37] In the XPS spectra of core-level C1s and Na1s (Figure 5g,i) of VCA-3 for SIBs, the presence of inorganic species (i.e., $ROCO_2Na/Na_2CO_3$, Na Auger, NaCl, etc.) can be detected in the SEI with an inorganic content of ≈33 at%. Hence, the SEI formed in the sodiated electrolyte consists of abundant organic species (≈67 at%) and partial inorganic components, which gives rise to the formation of a continuous phase with good flexibility.[38] Overall, the sodiated VCA-3 electrode possesses a flexible and stable SEI layer dominated by organic components, which can eliminate the reconstruction of the SEI layer and additional electrolyte decomposition upon the consecutive sodiation/desodiation process, thus leading to the prolonged cycling stability of the VCA-3 electrode.[39] However, as observed from Figure 6g,i of the cycled VCA-5 electrode for PIBs, the binding energies of $K2p_{3/2}$ and $K2p_{1/2}$ are spotted at ≈293.2 and ≈296.0 eV, together with two deconvoluted P2p peaks at ≈137.6 ($P2p_{3/2}$) and ≈138.8 eV ($P2p_{1/2}$). Notably, the potassiated electrolyte decomposes to form richer inorganic species (i.e., $ROCO_2K/K_2CO_3$, P2p, K2p, etc.) with a higher proportion of ≈51 at%, which induces the establishment of a well-balanced organic-inorganic SEI layer. The moderate amount of inorganic SEI species can facilitate a higher ionic conductivity and K^+ ion diffusion kinetics,[40] consistent with the superior rate performance of the VCA-5

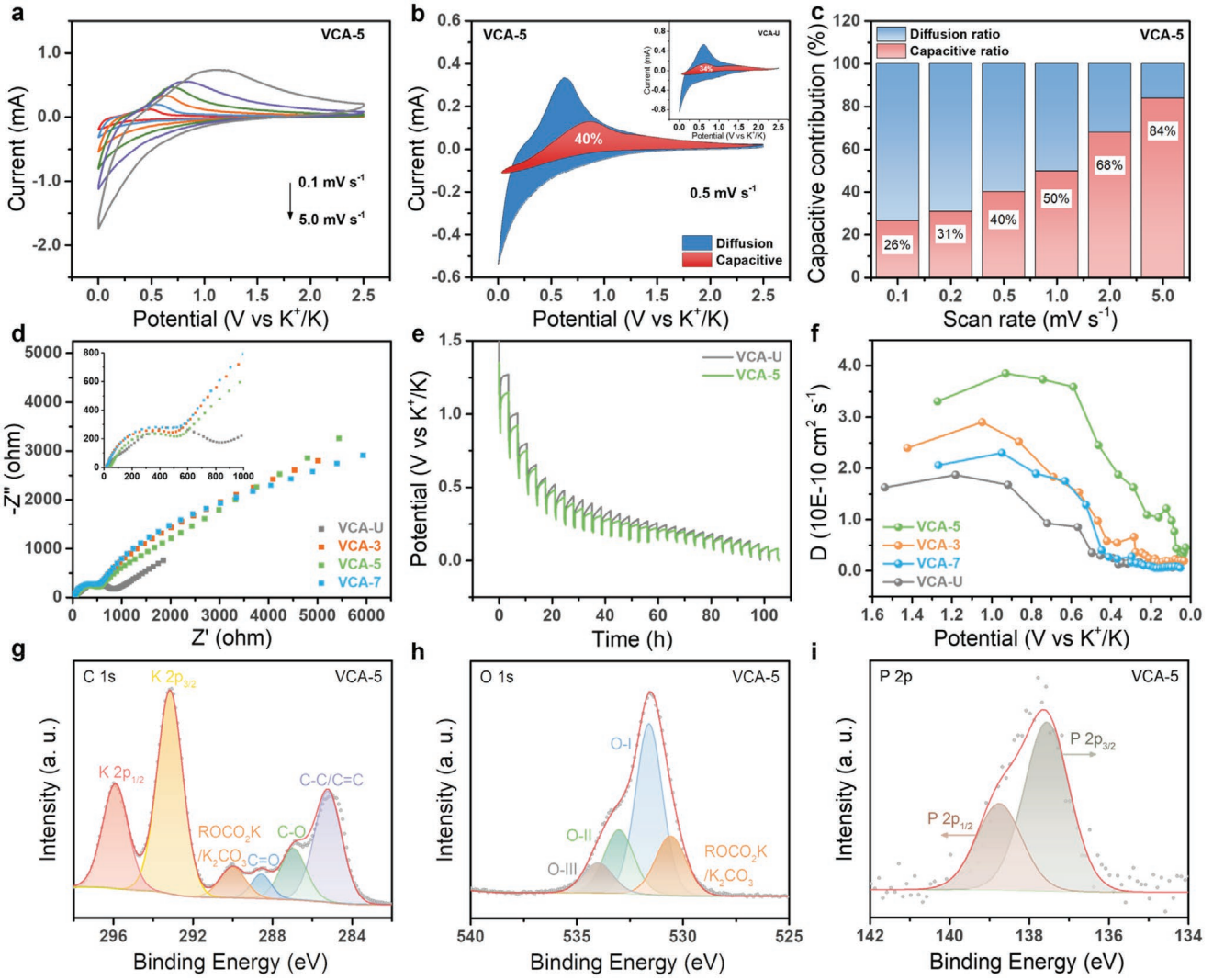

Figure 6. PIB analysis: a) CV curves at various scan rates from 0.1 to 5.0 mV s^{-1}. b) Separation of the capacitive and diffusion-controlled charges at 0.5 mV s^{-1}. c) Contribution ratios of the capacitive and diffusion-controlled charge at various scan rates. d) EIS analysis. e) GITT potential profiles of the discharging process. f) The potassium ion diffusion coefficients as a function of the state of the discharging process. Ex situ XPS spectra of g) fitted C 1s, h) O 1s, and i) P 2p core levels for the cycled electrode.

electrode for PIBs. For a quantitative comparison, the percentage of different species in the SEI layer formed on the sodiated and potassiated VCA electrodes is given in Figure S14, Supporting Information.

Ex situ HRTEM and SAED patterns were used to investigate the structural stability of the cycled electrodes in half cells of SIBs and PIBs after 100 cycles at 2.0 C, as shown in Figure S16, Supporting Information. The post-cycling VCA-3 (the best performing material for SIBs) electrode at the desodiated state still maintains the features of turbostratic structures and some short-range graphitic nanodomains with a similar average interlayer spacing (d_{002}) value (of 0.395 nm) compared to that of the pristine VCA-3, demonstrating the preservation of structural integrity without obvious insertion of sodium ions into graphitic nanodomains (see Figure S16c, Supporting Information). Meanwhile, the HRTEM image shown in Figure S16d, Supporting Information of the post-cycled VCA-5 electrode (the best performing material for PIBs) in the de-potassiated state still retains short-range ordered nanodomains with more graphitic structures. However, the interlayer spacing was slightly increased to 0.402 from 0.390 nm after 100 cycles, indicating that the high structural stability of VCA-5, and the few-layer graphitic nanodomains can reversibly expand/shrink due to potassium insertion/extraction. The SAED patterns (insets in Figure S16c,d, Supporting Information) before and after cycling still show no diffraction spots for VCA-3 and VCA-5 samples, which confirms a robust and stable structure for the post-cycling VCA electrodes for SIBs and PIBs. The unique hollow and vertically-aligned channels can effectively accommodate the volume change of electrodes during the sodiation/desodiation or potassiation/depotassiation processes, which contributes to retaining the structural integrity and alleviating the reduction in capacity.[41]

To fully compare and summarize the sodium/potassium storage mechanism of VCA electrodes, the schematic illustrations of capacitive- and diffusion-controlled mechanisms are depicted in **Figure 7**a,b. Based on the systematic verifications regarding the "adsorption-filling" sodium storage mechanism of hard carbons revealed by previous researchers[25,42] and our kinetic analysis, we can conclude that the sloping region above 0.1 V versus Na^+/Na of our VCA electrodes is derived from the capacitive-controlled Na^+ ion adsorption on defective sites, edges, surfaces, and functional groups, while the plateau region (≈0.1 V vs Na^+/Na) corresponds to the diffusion-controlled filling of Na^+ ions into nanovoids, as illustrated in Figure 7a. Furthermore, the diffusion-controlled storage behavior of SIBs and PIBs are distinctly different because the potassiation behavior of hard carbon in the low potential plateau region (≈0.3 V vs K^+/K) is similar to that of hard carbon for lithium storage; corresponding to the insertion of K^+ ions into graphitic nanodomains.[43] Ex situ HRTEM images provide the structural evidence highly favored for the existence of insertion/extraction of large-sized K^+ into/from the graphitic ordered nanodomains while there is an absence of insertion/extraction of Na^+ into/from the graphitic nanodomains in our VCAs. Hence, the "adsorption-insertion" potassium storage mechanism can be achieved (Figure 7b). With a precise control of cooling rate, defective structures with well-tuned homogenous channels of VCA-3 contributed to its superior sodium storage performance, while the well-tuned graphitic nanodomains of VCA-5 with enlarged interlayer spacings and moderate defects allow it to be an optimum electrode material for PIBs.

Inspired by the abovementioned results, it is expected that the as-prepared VCA-3 anode paired with a $Na_3V_2(PO_4)_3$ cathode could be an appealing candidate for sodium-ion full

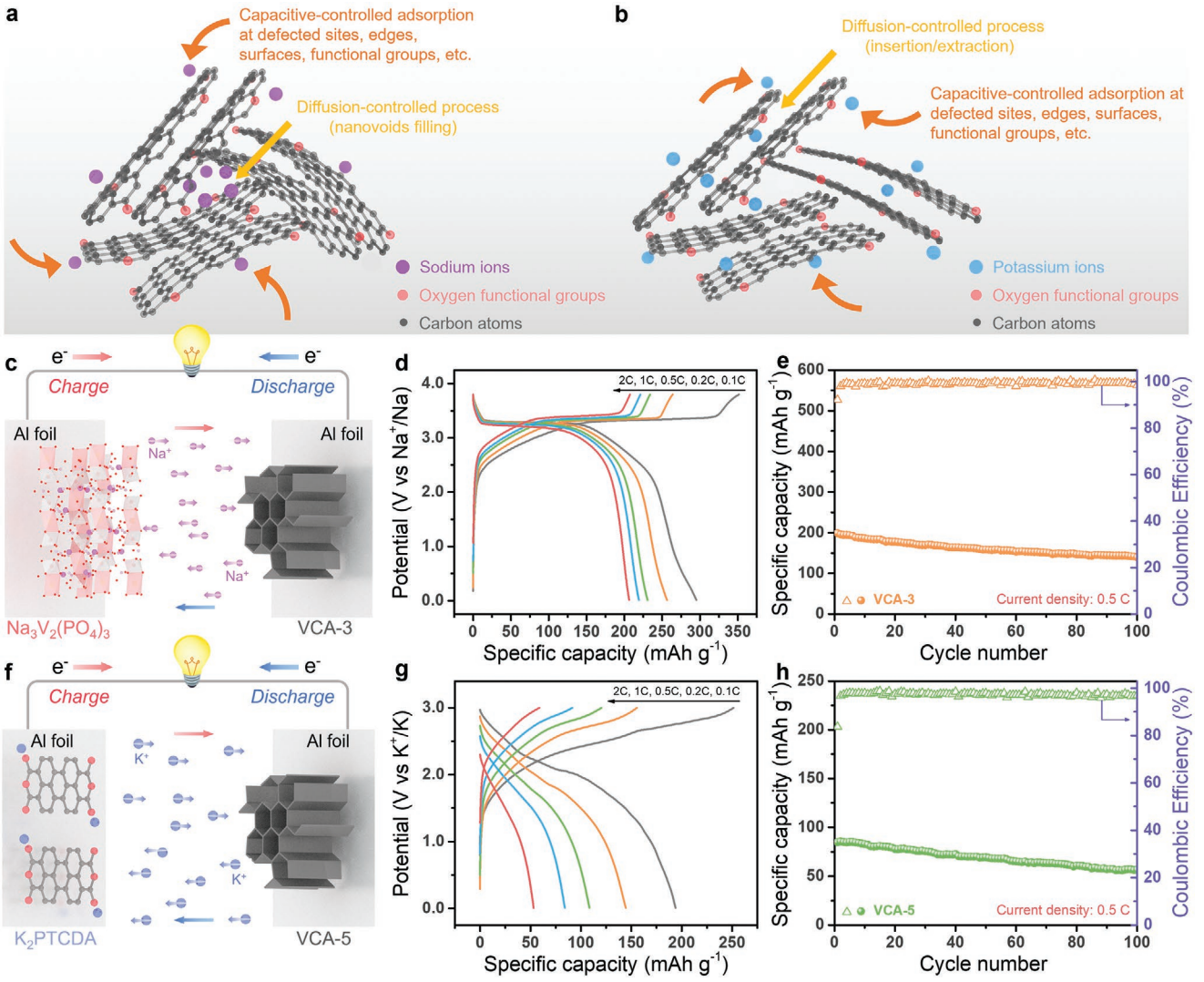

Figure 7. Schematic illustration of capacitive- and diffusion-controlled mechanisms of a) SIBs and b) PIBs. c) Schematic working principle, d) discharge/charge profiles at various current densities (each curve represents the first cycle at the corresponding C-rate), and e) cycling performance operated at 0.5 C of a VCA-3//$Na_3V_2(PO_4)_3$ sodium-ion full cell. f) Schematic working principle, g) discharge/charge profiles under different current densities, and h) cycling performance at 0.5 C of a VCA-5//K_2PTCDA potassium-ion full cell.

cells; its working principle is sketched in Figure 7c. Pre-cycling of the electrode materials was performed in advance, for the benefit of minimizing its polarization and irreversible effect in the initial discharge process. The remarkable rate performance of the VCA-3//$Na_3V_2(PO_4)_3$ sodium-ion full cell is shown in Figure 7d, reaching an ultrahigh reversible capacity of 295, 256, 231, 219, and 206 mAh g^{-1} (based on the weight of the anode) at current rates (C-rate) from 0.1 to 2 C tested in a voltage window of 0.01–3.80 V. The cycling performance and corresponding Coulombic efficiency of the Na-ion full battery are shown in Figure 7e. After 100 sodiation/desodiation cycles at 0.5 C, the full cell displays a good cyclability with a capacity retention of 71.3% which is higher than that of several reported sodium-ion full cells.[44] The energy density of VCA-3//$Na_3V_2(PO_4)_3$ full cell is calculated to be ≈220 Wh kg^{-1}, where its sufficient energy output is able to power an orange light-emitting diode (LED) as shown in the inset of Figure 7e. It is worth noting that our VCA-3//$Na_3V_2(PO_4)_3$ full cell synchronously manifests the superior capacity and energy density, which outperforms other previously reported sodium-ion full battery configurations (Table S4, Supporting Information). Additionally, the practical applications of VCA-5 were further evaluated by assembling K-ion full cell (VCA-5//K_2PTCDA) and its working mechanism is schematically illustrated in Figure 7f. Figure 7g shows the typical charge–discharge profiles of the K-ion full cell at current rates from 0.1 to 2 C in the voltage range of 0.01–3.00 V. The full cell exhibits a high discharge capacity (194 mAh g^{-1} at 0.1 C), a good rate capability (84 mAh g^{-1} at 1 C), and an acceptable cyclability at 0.5 C over 100 potassiation/depotassiation cycles (see Figure 7h). Intuitively, the inset of Figure 7h demonstrates the lighted green LED driven by one operated K-ion full cell, revealing its appealing potential for practical applications. The energy density of VCA-5//K_2PTCDA full-cell was estimated ≈118 Wh kg^{-1}, which is comparatively higher among some reported PIB full cells (see Table S5, Supporting Information).

3. Conclusions

In summary, we proposed a novel and facile controllable ice-templating strategy to fabricate CNC/PEO-derived VCA electrode materials with hierarchically tailored and vertically-aligned hollow channels. By gently controlling the cooling rate of the unidirectional ice-templating technique, the oxygen-functionality, ordered structures, defect densities, channel widths, as well as interlayer spacings of graphitic domains for VCAs have been tuned gradually to modulate the Na^+/K^+ storage behavior, thereby ensuring optimized ice-templated carbon micro/nanostructures suited for their application as stable SIB or PIB anode materials. With the aid of fine-tuning, VCA-3 exhibits a high reversible capacity (298 mAh g^{-1} at 0.1 C), superior long-term cycling stability (over 2000 cycles with 0.03% capacity fading per cycle) as anode materials for SIBs. When coupled with a $Na_3V_2(PO_4)_3$ cathode, the Na-ion full cell manifests a high energy density of ≈220 Wh kg^{-1} and a high-rate capability with a capacity of 206 mAh g^{-1} at 2 C. As an anode for PIBs, VCA-5 shows excellent rate capability (148 mAh g^{-1} at 2 C) and an extraordinary cyclability (82.7% capacity retention after 1000 cycles). Moreover, the K-ion full cell based on the VCA-5 and K_2PTCDA delivers a favorable energy density of ≈118 Wh kg^{-1} and a good cycling stability. The above-mentioned results demonstrate a practical pathway to tune electrochemical storage performance through a controllable ice-templating strategy which can be easily extended to a variety of other energy storage systems such as zinc-, calcium-, aluminum-, and magnesium-ion batteries, exhibiting its universal potential for the next-generation of energy storage systems. Benefiting from the renewability of the precursor and scalability at relatively low cost in the environmentally benign synthesis process, this work could offer an appealing route to promote large-scale applications of sustainable EVs and large-scale energy storage grids in the near future.

4. Experimental Section

Fabrication of VCAs via Unidirectional Ice-Templating Method: First, freeze-dried CNCs were obtained from filter paper (Whatman No.1) according to the acid-hydrolysis method previously reported by the authors' group.[45] In a typical synthesis procedure, an aqueous suspension of CNCs (12 mL, 100 mg mL^{-1}) was mixed with a PEO aqueous solution (48 mL, 25 mg mL^{-1}) under vigorous stirring for 24 h to form a homogenous suspension. The CNC/PEO suspension was poured into a cylindrical Teflon mold sitting on a copper rod in contact with a liquid nitrogen bath to achieve vertical unidirectional freezing of the composite suspension (Scheme 1). The cooling rate of the resulting suspension was monitored by a thermocouple inserted into the copper rod connected to a programmed proportional-integral-derivative temperature controller. The suspensions were frozen at constant cooling rates of 3, 5, and 7 K min^{-1}; for contrast, the suspension was frozen without the connection of the heat controller for the uncontrolled freezing. The CNC/PEO ice crystals were freeze-dried under vacuum for 24 h, followed by thermal annealing at 1300 °C in He for 2 h to obtain the VCAs. The as-obtained VCA anodes with the uncontrolled freezing, at the cooling rates of 3, 5, and 7 K min^{-1}, were designated as VCA-U, VCA-3, VCA-5, and VCA-7, respectively.

Materials Characterizations: The morphology and structure of the aerogels were investigated by SEM (JEOL IT300) and X-ray tomography (Xradia 520 Versa, Zeiss) with an accelerating voltage of 15 and 40 kV, respectively. TEM and SAED were performed at 200 kV on a JEOL 2100F TEM. XRD patterns were recorded using a diffractometer (D8 Advance, Bruker) with Cu-Kα radiation (λ = 0.154 nm). XPS measurements were obtained on an X-ray photoelectron spectrometer (K-Alpha, Thermo Fisher) with monochromatic Al-Kα as the excitation source. Raman spectroscopy data were collected on a Renishaw inVia spectrometer with 532 nm laser excitation (exposure time: 5 s; imaging microscope system at 50×). The specific surface areas and pore size distributions were determined using N_2 adsorption/desorption apparatus (TriStar II PLUS, Micromeritics) via BET method and non-local DFT. The post-tested SIBs/PIBs were disassembled in an argon-filled glove box, and then the VCA electrodes were cleaned in dimethyl carbonate (DMC) or diethyl carbonate (DEC) solution, respectively. These dried VCA electrodes were subsequently sealed in a vacuum transferring capsule to carefully avoid exposure to the air for conducting ex situ XPS measurements. The binding energy was calibrated with respect to the C_{1s} peak at 284.8 eV. For the ex situ TEM observations, the post-cycling VCA-3 and VCA-5 samples were rinsed with DMC and DEC to remove excessive salts for half cells of SIBs and PIBs, respectively. The dried VCA-3 and VCA-5 electrodes were uniformly dispersed in ethanol, and then the mixture solution was dropped onto TEM grids (carbon film-covered copper grids) for observations.

Electrochemical Measurements: For both SIBs and PIBs, the battery performances were tested on MTI CR2032 coin-type cells assembled in

an Argon-filled glovebox (LABstar, MBRAUN). The working electrode was composed of 80 wt% active materials (VCA-U, -3, -5, and -7), 10 wt% carbon black, and 10 wt% sodium alginates. The mixed slurry was blade-coated onto an aluminum foil and then dried under vacuum at 100 °C for 12 h. The mass loading of VCAs electrodes was controlled at 1.5–2.0 mg cm^{-2}. For the half cells of SIBs and PIBs, sodium or potassium metal adopted as the counter electrode, 1.0 M $NaClO_4$ in a mixture of ethylene carbonate (EC)/DMC (1:1, v/v) or 0.8 M KPF_6 in 1:1 v/v EC/DEC employed as the electrolyte, and glass fiber filters (Whatman GF/D) served as the separators. The GCD tests were conducted within the potential window of 0.01–2.5 V using a LAND-CT3001A multichannel battery test system. CV measurements (voltage range: 0.01–2.5 V, scan rates of 0.1, 0.2, 0.5, 1, and 2 mV s^{-1}) and EIS analysis (frequency range: 1000 kHz–0.01 Hz) of coin cells were performed on an Autolab PGSTAT204 electrochemical workstation. GITT measurements were performed by applying current pulses at 0.1 C for 0.5 h followed by a 3 h relaxation process on a battery test system (LAND-CT3001A). A sodium-ion full cell was assembled using VCA-3 as the anode and $Na_3V_2(PO_4)_3$ as the cathode in a CR2032 coin-type cell. After pre-potassiation of 3,4,9,10-perylene-tetracarboxylicacid-dianhydride (PTCDA) and pre-potassiation/depotassiation of VCA-5, the VCA-5//K_2PTCDA potassium-ion full cell was assembled in a CR2032 coin-type cell. The mass ratio of the cathode to anode was controlled at 2.9/1 and 2.2/1 in the Na- and K-ion full battery, respectively.

Supporting Information

Supporting Information is available from the Wiley Online Library or from the author.

Acknowledgements

J.W. and Z.X. contributed equally to this work. This work was supported by a grant from the Engineering and Physical Sciences Research Council (EP/V002651/1), Chemical Imaging Facility at the University of Bristol (equipment funded by EPSRC under Grant "Atoms to Applications" EP/K035746/1). The authors appreciate the assistance from Dr. Cynthia Adu and Yusuf Mahadik for the set-up of the unidirectional ice-templating equipment. The authors also would like to thank Zhenyu Guo for accessing XRD and the supply of the PTCDA cathode and Xin Song and Gang Cheng for assistance with the SEM images. J.W. and Z.X. acknowledge the China Scholarship Council for their Ph.D. scholarships.

Conflict of Interest

The authors declare no conflict of interest.

Data Availability Statement

The data that support the findings of this study are available in the supplementary material of this article.

Keywords

hard carbon anodes, sodium/potassium-ion full cells, sustainable aerogels, unidirectional ice-templating

Received: October 26, 2021
Revised: December 8, 2021
Published online:

[1] D. Davies, M. Verde, O. Mnyshenko, Y. Chen, R. Rajeev, Y. Meng, G. Elliott, *Nat. Energy* **2019**, *4*, 42.
[2] a) A. Eftekhari, *ACS Sustainable Chem. Eng.* **2019**, *7*, 5602; b) S. Ding, B.-X. Zhou, C. Chen, Z. Huang, P. Li, S. Wang, G. Cao, M. Zhang, *ACS Nano* **2020**, *14*, 9626.
[3] F. Heredia, A. L. Martinez, V. Surraco Urtubey, *J. Energy Nat. Resour. Law* **2020**, *38*, 213.
[4] X. Zou, P. Xiong, J. Zhao, J. Hu, Z. Liu, Y. Xu, *Phys. Chem. Chem. Phys.* **2017**, *19*, 26495.
[5] X. Wu, Y. Chen, Z. Xing, C. W. K. Lam, S.-S. Pang, W. Zhang, Z. Ju, *Adv. Energy Mater.* **2019**, *9*, 1900343.
[6] J. Zhou, X. Lian, Y. You, Q. Shi, Y. Liu, X. Yang, L. Liu, D. Wang, J. H. Choi, J. Sun, *Adv. Funct. Mater.* **2021**, *31*, 2102047.
[7] G. Yoon, H. Kim, I. Park, K. Kang, *Adv. Energy Mater.* **2017**, *7*, 1601519.
[8] R. Rajagopalan, Y. Tang, X. Ji, C. Jia, H. Wang, *Adv. Funct. Mater.* **2020**, *30*, 1909486.
[9] J. Wang, B. Wang, X. Liu, J. Bai, H. Wang, G. Wang, *Chem. Eng. J.* **2020**, *382*, 123050.
[10] Z. Zhu, F. Liang, Z. Zhou, X. Zeng, D. Wang, P. Dong, J. Zhao, S. Sun, Y. Zhang, X. Li, *J. Mater. Chem. A* **2018**, *6*, 1513.
[11] a) E. Irisarri, A. Ponrouch, M. Palacin, *J. Electrochem. Soc.* **2015**, *162*, A2476; b) Z. Jian, Z. Xing, C. Bommier, Z. Li, X. Ji, *Adv. Energy Mater.* **2016**, *6*, 1501874; c) J. Yang, Z. Ju, Y. Jiang, Z. Xing, B. Xi, J. Feng, S. Xiong, *Adv. Mater.* **2018**, *30*, 1700104.
[12] S. Deville, E. Saiz, A. P. Tomsia, *Acta Mater.* **2007**, *55*, 1965.
[13] a) R. Dash, Y. Li, A. J. Ragauskas, *Carbohydr. Polym.* **2012**, *88*, 789; b) S. A. Barr, E. Luijten, *Acta Mater.* **2010**, *58*, 709.
[14] H. Chen, A. Pei, J. Wan, D. Lin, R. Vilá, H. Wang, D. Mackanic, H.-G. Steinrück, W. Huang, Y. Li, *Joule* **2020**, *4*, 938.
[15] a) S. J. Eichhorn, *Soft Matter* **2011**, *7*, 303; b) E. J. Foster, R. J. Moon, U. P. Agarwal, M. J. Bortner, J. Bras, S. Camarero-Espinosa, K. J. Chan, M. J. Clift, E. D. Cranston, S. J. Eichhorn, D. M. Fox, W. Y. Hamad, L. Heux, B. Jean, M. Korey, W. Nieh, K. J. Ong, M. S. Reid, S. Renneckar, R. Roberts, J. A. Shatkin, J. Simonsen, K. Stinson-Bagby, N. Wanasekara, J. Youngblood, *Chem. Soc. Rev.* **2018**, *47*, 2609.
[16] S. Deville, E. Saiz, R. K. Nalla, A. P. Tomsia, *Science* **2006**, *311*, 515.
[17] S. Mueller, C. Weder, E. J. Foster, *Green Mater.* **2014**, *2*, 169.
[18] P. Lu, Y. Sun, H. Xiang, X. Liang, Y. Yu, *Adv. Energy Mater.* **2018**, *8*, 1702434.
[19] a) L. G. Cançado, A. Jorio, E. M. Ferreira, F. Stavale, C. A. Achete, R. B. Capaz, M. V. D. O. Moutinho, A. Lombardo, T. Kulmala, A. C. Ferrari, *Nano Lett.* **2011**, *11*, 3190; b) A. C. Ferrari, D. M. Basko, *Nat. Nanotechnol.* **2013**, *8*, 235.
[20] F. Xie, Z. Xu, A. C. S. Jensen, H. Au, Y. Lu, V. Araullo-Peters, A. J. Drew, Y.-S. Hu, M.-M. Titirici, *Adv. Funct. Mater.* **2019**, *29*, 1901072.
[21] G. Ma, K. Huang, J.-S. Ma, Z. Ju, Z. Xing, Q.-c. Zhuang, *J. Mater. Chem. A* **2017**, *5*, 7854.
[22] a) H. Au, H. Alptekin, A. C. S. Jensen, E. Olsson, C. A. O'Keefe, T. Smith, M. Crespo-Ribadeneyra, T. F. Headen, C. P. Grey, Q. Cai, A. J. Drew, M.-M. Titirici, *Energy Environ. Sci.* **2020**, *13*, 3469; b) J. M. Stratford, A. K. Kleppe, D. S. Keeble, P. A. Chater, S. S. Meysami, C. J. Wright, J. Barker, M.-M. Titirici, P. K. Allan, C. P. Grey, *J. Am. Chem. Soc.* **2021**, *143*, 14274.
[23] B. Cao, H. Liu, B. Xu, Y. Lei, X. Chen, H. Song, *J. Mater. Chem. A* **2016**, *4*, 6472.
[24] Z. Xu, F. Xie, J. Wang, H. Au, M. Tebyetekerwa, Z. Guo, S. Yang, Y.-S. Hu, M.-M. Titirici, *Adv. Funct. Mater.* **2019**, *29*, 1903895.
[25] D. Stevens, J. Dahn, *J. Electrochem. Soc.* **2000**, *147*, 1271.
[26] X. Xiong, C. Yang, G. Wang, Y. Lin, X. Ou, J.-H. Wang, B. Zhao, M. Liu, Z. Lin, K. Huang, *Energy Environ. Sci.* **2017**, *10*, 1757.
[27] Z. Jian, W. Luo, X. Ji, *J. Am. Chem. Soc.* **2015**, *137*, 11566.

[28] a) W. Zhang, W. K. Pang, V. Sencadas, Z. Guo, *Joule* **2018**, *2*, 1534; b) J. Zhao, X. Zou, Y. Zhu, Y. Xu, C. Wang, *Adv. Funct. Mater.* **2016**, *26*, 8103.
[29] Z. Sun, X. L. Wu, J. Xu, D. Qu, B. Zhao, Z. Gu, W. Li, H. Liang, L. Gao, Y. Fan, *Small* **2020**, *16*, 1907670.
[30] H. Zhang, H. He, J. Luan, X. Huang, Y. Tang, H. Wang, *J. Mater. Chem. A* **2018**, *6*, 23318.
[31] H. Yang, R. Xu, Y. Yao, S. Ye, X. Zhou, Y. Yu, *Adv. Funct. Mater.* **2019**, *29*, 1809195.
[32] a) D. Chao, C. Zhu, P. Yang, X. Xia, J. Liu, J. Wang, X. Fan, S. V. Savilov, J. Lin, H. J. Fan, *Nat. Commun.* **2016**, *7*, 12122; b) J. Wang, J. Polleux, J. Lim, B. Dunn, *J. Phys. Chem. C* **2007**, *111*, 14925; c) Z. Chen, V. Augustyn, X. Jia, Q. Xiao, B. Dunn, Y. Lu, *ACS Nano* **2012**, *6*, 4319.
[33] S. Wang, Y. Fang, X. Wang, X. W. Lou, *Angew. Chem., Int. Ed.* **2019**, *58*, 760.
[34] a) C. Bommier, T. W. Surta, M. Dolgos, X. Ji, *Nano Lett.* **2015**, *15*, 5888; b) J. Zhang, H. Yuan, Y. Huang, S. Kan, Y. Wu, M. Bu, Y. Liu, P. He, H. Liu, *Chem. Eng. J.* **2021**, *417*, 128097.
[35] a) A. Mahmood, S. Li, Z. Ali, H. Tabassum, B. Zhu, Z. Liang, W. Meng, W. Aftab, W. Guo, H. Zhang, *Adv. Mater.* **2019**, *31*, 1805430; b) Y. Liu, Y. X. Lu, Y. S. Xu, Q. S. Meng, J. C. Gao, Y. G. Sun, Y. S. Hu, B. B. Chang, C. T. Liu, A. M. Cao, *Adv. Mater.* **2020**, *32*, 2000505.
[36] B. Wang, F. Yuan, Q. Yu, W. Li, H. Sun, L. Zhang, D. Zhang, Q. Wang, F. Lai, W. A. Wang, *Energy Storage Mater.* **2021**, *38*, 329.
[37] D. Hulicova-Jurcakova, M. Seredych, G. Q. Lu, T. J. Bandosz, *Adv. Funct. Mater.* **2009**, *19*, 438.
[38] F. Xie, Z. Xu, Z. Guo, M.-M. Titirici, *Prog. Energy* **2020**, *2*, 042002.
[39] Z. Xu, Z. Guo, R. Madhu, F. Xie, R. Chen, J. Wang, M. Tebyetekerwa, Y.-S. Hu, M. Titirici, *Energy Environ. Sci.* **2021**, *14*, 6381.
[40] S. U. Yoon, H. Kim, H.-J. Jin, Y. S. Yun, *Appl. Surf. Sci.* **2021**, *547*, 149193.
[41] B. Cao, Q. Zhang, H. Liu, B. Xu, S. Zhang, T. Zhou, J. Mao, W. K. Pang, Z. Guo, A. Li, *Adv. Energy Mater.* **2018**, *8*, 1801149.
[42] Y. Li, Y. S. Hu, M. M. Titirici, L. Chen, X. Huang, *Adv. Energy Mater.* **2016**, *6*, 1600659.
[43] L. F. Zhao, Z. Hu, W. H. Lai, Y. Tao, J. Peng, Z. C. Miao, Y. X. Wang, S. L. Chou, H. K. Liu, S. X. Dou, *Adv. Energy Mater.* **2021**, *11*, 2002704.
[44] a) S. Komaba, W. Murata, T. Ishikawa, N. Yabuuchi, T. Ozeki, T. Nakayama, A. Ogata, K. Gotoh, K. Fujiwara, *Adv. Funct. Mater.* **2011**, *21*, 3859; b) X. Xie, K. Kretschmer, J. Zhang, B. Sun, D. Su, G. Wang, *Nano Energy* **2015**, *13*, 208.
[45] J. Wang, T. R. Pozegic, Z. Xu, R. Nigmatullin, R. L. Harniman, S. J. Eichhorn, *Compos. Sci. Technol.* **2019**, *182*, 107744.